SEMI-AUTOMATED SEGMENTATION AND QUANTIFICATION OF MITRAL ANNULUS AND LEAFLETS FROM TRANSESOPHAGEAL 3-D ECHOCARDIOGRAPHIC IMAGES

MIGUEL SOTAQUIRA,* MAURO PEPI,[†] LAURA FUSINI,[†] FRANCESCO MAFFESSANTI,[†‡] ROBERTO M. LANG,[‡] and ENRICO G. CAIANI*

*Dipartimento di Elettronica, Informazione e Bioingegneria, Politecnico di Milano, Milan, Italy; [†]Centro Cardiologico Monzino IRCCS, Milan, Italy; and [‡]Noninvasive Cardiac Imaging Laboratory, University of Chicago, Chicago, IL, USA

INTRODUCTION

The mitral valve (MV) is located in the left atrioventricular groove and prevents the systolic backflow from the left ventricle (LV) to the left atrium (LA). The mitral annulus (MA) is one of its anatomic components, a fibroelastic ring with a three-dimensional (3-D) saddle shape to which the anterior and posterior mitral leaflets (ML) attach (Muresian 2009). The quantification of MA and ML morphology is valuable for the diagnosis, treatment and follow-up of patients with MV disease (Vergnat et al. 2011; Grewal et al. 2009; Maffessanti et al. 2011). Transthoracic echocardiography is the standard imaging modality used to evaluate patients with MV disease. Recently, the advent of real-time 3-D transesophageal echocardiography (RT3-D TEE) has

enabled a more accurate morphologic and quantitative assessment of the MV apparatus, compared with conventional two-dimensional (2-D) or transthoracic 3-D ultrasound techniques, thus becoming the clinical standard for the pre-operative assessment of the MV (Grewal et al. 2009; Maffessanti et al. 2011). Despite its extended use, quantification of morphologic MA and ML parameters from RT3-D TEE data sets remains a challenge, and commonly it is performed using strategies that rely on manual and time-consuming segmentation procedures (Vergnat et al. 2011; Watanabe et al. 2006; Song et al. 2006).

Several semi-automatic approaches have been proposed to obtain more reproducible results and less cumbersome analyses. Schneider et al. (2010) proposed a semi-automatic method for the segmentation of the MA during systole, with the hypothesis that the annulus lies in the region where the thin-tissue of the leaflets is attached to the thicker-tissue of the ventricular walls. However, such an assumption is not valid in the anterior

Address correspondence to: Enrico G. Caiani, PhD, Politecnico di Milano, P.zza L. da Vinci 32, 20133 Milan, Italy. E-mail: enrico.caiani@polimi.it

annular portion, which prevents the correct application of a thin-tissue detector and an evolving contour to segment the MA. In Schneider et al. (2012), the previous approach is extended to the dynamic segmentation of the MA (from diastole to systole), using a modified optical flow approach; however, the method relies on the same assumptions of the morphology of the MA near the anterior annular portion. Pouch et al. (2012) combine an active contour guided segmentation followed by a deformable model approach to segment both the MA and ML, but an adequate orientation of the MV within the pyramidal volume data set is required to achieve accurate segmentations, thus limiting the applicability of this approach. Burlina et al. (2010), Schneider et al. (2011) and Mansi et al. (2012) made use of model-based methods that incorporate geometric, morphologic or mechanical constraints that were dependent on the training sets and therefore could not be fully verified in the presence of MV pathologies. Ionasec et al. (2010) made use of machine learning techniques to delineate the 4-D MA; the method is accurate and has been thoroughly tested (1516 RT3-D TEE data sets), but it requires an extensive training database of manually delineated features, which makes it both dependent on the training sets and inaccessible to most. In addition, none of the proposed methods fully computes and exploits the local morphology of ML thickness and tenting, thus limiting the clinical applicability of those approaches.

In this article, we thoroughly describe and validate a novel semi-automated approach that requires minimal user interaction for segmenting the MA, the ML and the CL from RT3-D TEE data sets in the closed MV configuration (systolic phase), which allows the computation of novel quantitative parameters, such as regional leaflet thickness and regional tenting height. The accuracy and reproducibility of the MA and ML segmentation and of the computed parameters were tested on a heterogeneous data set of 33 patients; additionally, the potential clinical applicability of this approach in the presence of MV pathologies was also tested. Preliminary results of the proposed approach on a smaller group of patients were presented in Sotaquira et al. (2013).

METHODS: MITRAL VALVE SEGMENTATION

The proposed method operates on the RT3-D TEE image by first deriving the MA from a set of user-defined points, and then constructing the ML 3-D surface in a fully automated fashion. For MA detection, we pro-pose a modified block-matching algorithm inspired by the work of Nevo et al. (2007), able to track in 3-D space the position of the annular points starting from the set of annular locations defined by the user. This modified algorithm involves the use of image cross-correlation and the

enhancement of annular locations using morphologic operations. Next, using a graph-based approach, the ML is automatically delineated from the set of detected annular points. Finally, the 3-D polygonal mesh representations of both MA and ML are computed, including a semi-automatic procedure for the coaptation line detection, and the set of morphologic parameters is then quantified.

Figure 1 depicts the flow chart for the proposed algo-rithm. Such steps are described in detail in the following sections.

Manual initialization

After selecting a frame at closed valve (end-systole), the user navigates the 3-D volume and selects three points: one at the anterior (A) and posterior (P) annular locations and one in the left atrium (LA) (Fig. 2a). The mid-point between A and P defines the origin of the coordinate system. The axis in the longitudinal direction, perpendicular to the axis connecting A and P and pointing in the atrial direction, is then used to obtain a stack of 36 rotational cut-planes (inter-plane angular spacing of 5°). The LA point ensures that each plane in the stack is correctly oriented in 2-D space (*i.e.,* with the LA lying on top of the valvular plane and the LV on the bottom), regardless of the orientation of the MV within the acquired 3-D volume.

Finally, the user subsequently defined an additional set of 6 annular points:

- Antero-lateral (Al) and Postero-medial (Pm) points, selected from a cut-plane orthogonal to that containing the A and P points and passing through the origin of the coordinate system (Fig. 2b);
- 4 points on the anterior portion of the MA on four cut-planes in the stack, symmetrically positioned (at $\pm$ 15° and $\pm$ 30°) around A (Fig. 2c).

Mitral annulus segmentation

Given the stack of 36 rotational cut-planes and the eight previously initialized annular points, the task is to locate in 3-D space the remaining 64 annular points P_i ($i = 1…64$) on the non-initialized semi-planes (each of them consisting of one half of the original cut-planes, and thus containing one annular point). For each of these semi-planes, a region-of-interest (ROI) is automatically selected and centered on the initialized point in the semi-plane closer to P_i (Fig. 3a). A region-of-search (ROS) is automatically defined on the semi-plane con-taining P_i (centered on the ROI position) (Fig. 3b) and a weighted normalized cross-correlation (WNCC)(Bohs and Trahey 1991) between ROI (the template) and ROS images is then computed (Fig. 3c), where the weight corresponds to a Gaussian function. The ROI size was defined heuristically and set to 24 $\times$ 28 mm^2,
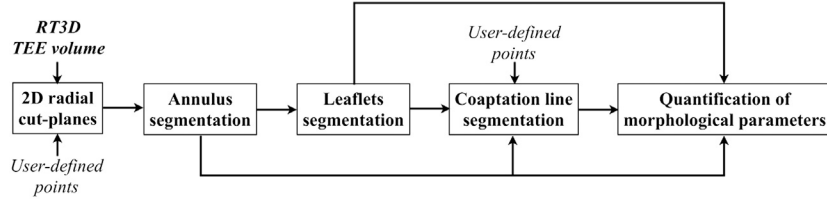
Fig. 1. Flow chart for the MV segmentation and quantification algorithm.

thus being large enough to identify a unique region, but small enough not to suffer too much from deformation of the block content over the multiple 2-D semi-planes. The ROS size was set to 30×50 mm^2 based on the maximum expected spatial displacement (in vertical and horizontal directions) of the annular points.

1 Junction-enhanced (JE) image. This procedure enhances the regions in ROS (Fig. 3b) that satisfy the thin-thick criterion, (*i.e.,* regions were the thin tissue of the leaflets is attached to the thicker tissue of the ventricular wall as visible on the 2-D cut-plane). The first step in the computation is to estimate the average leaflet thickness from initialized planes. To do so, for each user-defined point an inner region of the ROI containing a portion of the leaflet is automatically extracted from the correspond-ing semi-plane and used to compute two feature images:

- Leaflet medial axis: Obtained by first using the gray-level intensities of the selected portion as costs in a

2-D graph and then applying a dynamic programming algorithm (Amini et al. 1990; van Stralen et al. 2008; Nevo et al. 2007) that automatically computes the leaflet medial axis.

- Leaflet binary mask: Obtained using an unsupervised spatial fuzzy segmentation algorithm (Chuang et al. 2006; Abdel-Dayem and El-Sakka 2007) that computes a probability image (with values ranging between zero and one) representing the probability that a pixel belongs to a specific cluster, taking into account the existing correlation between neighboring

pixels. As in this application the cluster of pixels belonging to the ML was the object of interest, the corresponding binary mask was obtained by thresholding the probability image, with a threshold equal to 0.4 defined empirically from the analysis of the 33 patients. Once the leaflet binary mask was obtained, the Euclidean distance (from mask's inner points to its boundary) was computed. From these images, the leaflet thickness was obtained by averaging the Euclidean distances along the medial axis of each of the leaflet sections.

The second step in the computation of the JE image is to apply a morphology-based approach to enhance the annular locations, based on the assumption that they correspond to regions where objects with a thickness similar to that of the leaflets attach to thicker objects. To this aim, a binary mask $\mathbf{M}_{ROS}$ (Fig. 3d), is obtained from ROS (using the same fuzzy segmentation algorithm mentioned previously), from which two additional binary images are computed:

$$\mathbf{M}_{THICK} = \mathbf{M}_{ROS} \circ \mathbf{L} \qquad (1)$$

$$\mathbf{M}_{THIN} = XOR(\mathbf{M}_{ROS}, \mathbf{M}_{THICK}) \qquad (2)$$

$\mathbf{M}_{THICK}$ (Fig. 3e) contains only the thick tissue, and is the result of applying a morphologic opening (symbol $\circ$ in eqn [1]) operation on $\mathbf{M}_{ROS}$ using a circular structuring element, $\mathbf{L}$, with its diameter equal to the average leaflet thickness. $\mathbf{M}_{THIN}$, contains only the thin
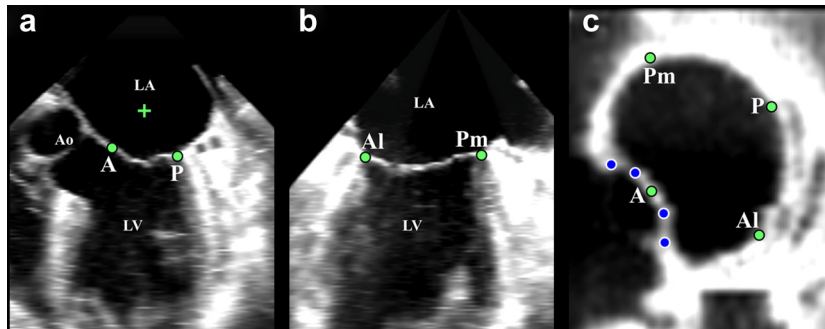

Fig. 2. Location of initialization points for the MA segmentation algorithm (see text for details). (a) A, P and LA points; (b) Al and Pm points; (c) atrial view of the MV with a projection of all the initialized points. Note the denser initialization of the anterior region. Ao: Aortic valve.
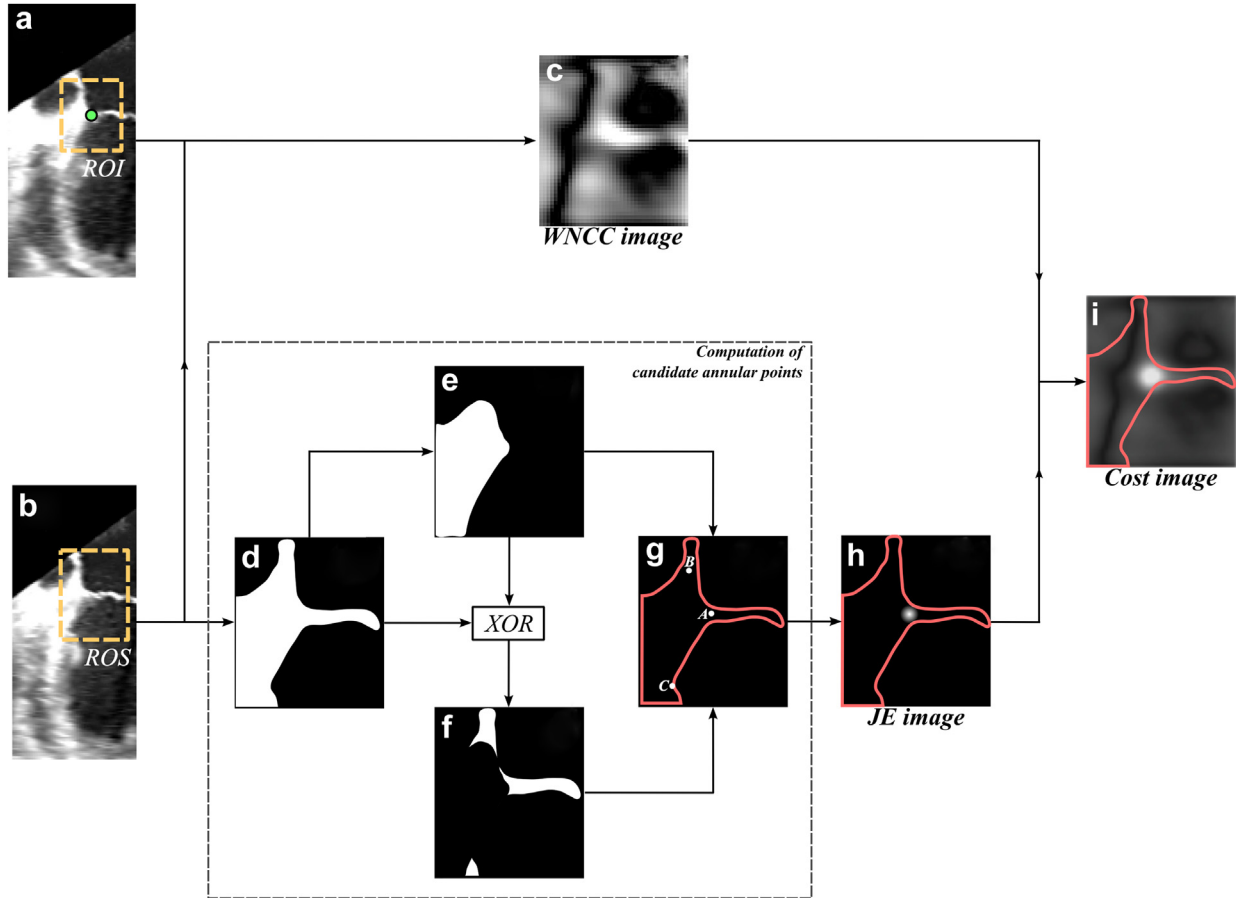
Fig. 3. Computation of cost-image on a non-initialized semi-plane (see text for details). Semi-planes containing ROI and ROS images (a, b); (c) computed WNCC image; (d) M_{ROS}: Binary mask of ROS image; (e) M_{THICK}: thick-tissue mask; (f) M_{THIN}: thin-tissue mask; (g) resulting candidate annular locations (A, B, and C); (h) JE image; (i) computed cost image.

tissue and is the result of an XOR logical operation between $\mathbf{M}_{THICK}$ and $\mathbf{M}_{ROS}$ (Fig. 3f).

Finally, for each binary object in $\mathbf{M}_{THIN}$, the centroid of the set of points closer to $\mathbf{M}_{THICK}$ (in the Euclidean sense) is automatically computed. The centroids A, B and C in Figure 3g are an example of this computation, where it is worth noting that, despite being artifacts owing to the local tissue morphology, B and C also satisfy the thin-thick tissue junction criterion. To remove these false annular locations, the orientation of each of the corresponding binary objects in $\mathbf{M}_{THIN}$ is computed as the mean angle with the horizontal axis of points belonging to the object, and only the structure with the most horizontal orientation is kept (*i.e.,* only A in Figure 3g remains). This criterion can be applied since the initialized LA point ensures that in the cut-planes the ML exhibits an almost-horizontal orientation. The remaining point is then convolved with a 2-D Gaussian kernel that emulates the uncertainty in the position of the detected junction, thus resulting in the JE image (Fig. 3h), normalized between zero and one, where pixel

values closer to one denote higher probability of belonging to the annulus.

2 Cost image computation and MA detection. The MA detection algorithm makes extensive use of the Dijkstra (Dijkstra 1959) optimal path search algorithm. Generically, a graph $G = <V,E>$ is a structure consisting of a set of nodes V and a set of edges E between connected pairs of nodes, with the latter usually having a cost (*i.e.,* being numerically weighted). Dijktra's algorithm solves the problem of finding the minimum-cost path to connect-ing a pair of "source" and "target" nodes in G. To do so, the algorithm starts at the "source" node and iterates through its neighbors; on each iteration, it computes and stores both the cumulative cost and the id of the node with the minimum cost. Once the "target" node is reached, the algorithm backtracks through the minimum cost path until it reaches the "source" node, thus con-structing the desired connected path.

With the estimation of the WNCC and the JE images, we compute a set of cost images and apply

Dijkstra's algorithm to compute the remaining annular locations. First, the WNCC and JE images are averaged together, thus resulting in the cost image C (Fig. 3i). This procedure, along with the use of the eight user-defined annular points, adds robustness to the detection of points even in the anterior annular portion. After repeating this step on each of the semi-planes, a set of 64 cost images is obtained. This set is further divided into eight different subsets s_m (of M rows, N columns and O slices each), each of them delimited by a pair of initialized points. Both s_m and the corresponding position of the initialized pair of points are then used to construct a directed weighted graph on which the Dijkstra shortest path algorithm is applied, thus automatically computing the remaining annular locations.

In the proposed approach, each graph (Fig. 4) will have a set of O layers (corresponding to each of the O slices in s_m) delimited by a pair of *start* and *end* nodes (defined by the 2-D locations of the initialized points). The voxels, v_{ijk}, in s_m act as the n_{ijk} nodes in the directed graph, whereas their corresponding intensity-transformed values, $1-v_{ijk}$, define the corresponding edge costs, thus ensuring that annular locations will be associated with non-negative edge values closer to zero.

The directional edges in the graph are defined by using a radial connectivity constraint applied both to *start* and *end* nodes, as well as to internal nodes:

- Assuming that the 2-D locations, in cost-image coordinates, of the pair of initialized points are (x_s, y_s) and (x_e, y_e), the *start* and *end* nodes will be connected to nodes in the first and O-th layers within a circular neighborhood[1] of radius r and centered on the locations (x_s, y_s) and (x_e, y_e) of the corresponding first and O-th slices in s_m.
- In the same fashion, internal edges between consecutive layers in the graph are defined by connecting each node n_{ijk} ($k = 1 \ldots O\text{-}1$) on the k-th layer with the corresponding set of nodes in the $k + 1$-th layer that lie within a neighborhood of radius r of the corresponding slices in s_m.

Once applied to the Dijkstra algorithm on the corresponding graphs, the set of 64 unknown annular locations is then obtained and transformed from 2-D cost image coordinates into the corresponding 3-D coordinates, which, along with the eight initialized points, represent the segmented MA. The use of this graph-based algorithm to construct the annulus, instead of the simple use of

global maximum of individual cost-images, ensures spatial smoothness and continuity between the detected points.

The annular contour is now represented by the final set of 72 annular points. However, given the noise present on each of the cut-planes, an additional step constituted by fourth order Fourier approximation was introduced to both reduce the potential misplacement of some points and to ensure better correspondence with the morphologic 3-D saddle shape of the MA.

ML segmentation

This fully-automated step takes as input the set of 3-D fitted annular locations (72 points) previously computed, along with the corresponding stack of 36 radial cut-planes. It exploits the fact that, on each plane, the gray-level intensity distribution along the leaflet cross-section exhibits higher values near the center of the leaflet.

ML segmentation starts by first computing the negative image of each cut-plane, thus ensuring that pixels near the center of the leaflet will have lower intensity values (Fig. 5, left); then, a 2-D directed weighted graph is constructed using the corresponding intensity values as edge weights. Finally, the minimum cost path between the corresponding set of annular points is computed using the Dijkstra algorithm, resulting in the leaflets medial-axis (Fig. 5, left, continuous line). The set of computed medial-axes (one for each radial cut-plane) is the output of the algorithm and corresponds to a 3-D point cloud that closely follows the 3-D medial surface of the mitral leaflets.

Semi-automatic detection of CL

The CL semi-automatic delineation is based on the fact that this line corresponds to the regions on the ML mesh that exhibit high local tenting values. A constrained conforming Delaunay triangulation (Shewchuk 2000) is then applied to both the 3-D MA fit points and the ML points cloud to obtain their corresponding 3-D mesh representations. Then, the local tenting height, defined as the vertex-to-vertex distance between the MA and ML meshes (both having the same number of vertices, sharing the same *x, y* coordinates and differing only in the *z* coordinate), is computed and visualized as color overlay on a 3-D rendering of both the original RT3-D TEE volume and the ML mesh (Fig. 6a).

On this 3-D image, the user initializes some points (between 4 and 6) on the ML mesh along the CL, where the local tenting height color information simplifies the selection (Fig. 6b). A weighted graph is then constructed by using the 1-ring connectivity of each vertex on the mesh and with the edge weights defined by the corresponding vertex tenting height. Finally a minimum cost

---

[1] In the implementation of the algorithm, this radial connectivity was determined heuristically and set to 5 mm, and corresponds to the maximum expected displacement (horizontal and vertical) of the annular point between consecutive slices.
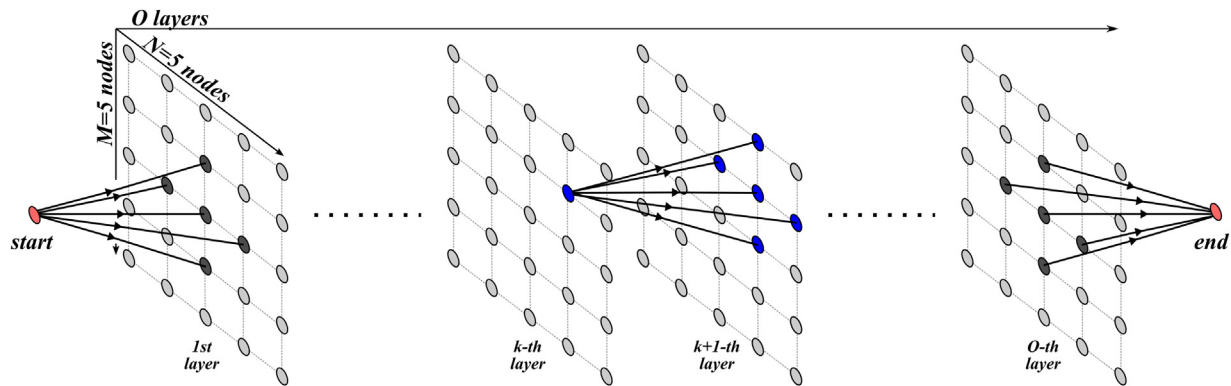
Fig. 4. A 3-D graph used for computing annular points using Dijkstra algorithm (Dijkstra, 1959). A simple structure of O layers and 5 × 5 nodes/layer and a radial connectivity constraint of 1 pixel are assumed in this example. The directed edges for the "start" and "end" nodes, as well as for a node in the k-th layer, are depicted as continuous black lines with arrows.

path calculation, using Dijkstra's algorithm, is performed between consecutive pairs of initialized points, thus obtaining a complete detection of the CL. The A and P ML representations are then obtained by cutting the ML mesh through the computed CL (Fig. 6c).

Quantification of morphologic parameters

Several conventional morphologic parameters (Caiani et al. 2011) were then computed from the 3-D MA contour and its mesh representation (obtained by computing the union of the triangles connecting the MA with its centroid) as well as from the ML mesh: (i) MA perimeter; (ii) A-P diameter (the axis starting from the saddle horn—the highest point in the MA measured in the orthogonal direction to the MV plane—and passing through MA centroid); (iii) Al-Pm diameter (perpendicular to the A-P axis and passing through MA centroid); (iv) MA height (the height of the MA bounding box); (v) MA 3-D surface; (vi) MA 2-D projected area; (vii) ML 3-D surface. In addition, a set of novel morphologic parameters, derived from the quantification of ML local thickness and ML tenting, was also computed from the mesh representations: (viii) ML mean thickness, obtained

as the average of the ML local thickness computed for each vertex of the ML mesh as twice the value of the distance transformed through the leaflets medial-axis on each cut-plane (Fig. 5, right); (ix) ML tenting volume (defined as the volume enclosed by MA and ML meshes); (x and xi) maximum and mean tenting height, both obtained from the ML local tenting height pattern computed for each vertex in the ML mesh (as explained in the previous section).

Population, validation protocol and statistical analysis

Data from patients enrolled at the University of Chicago Hospitals (Chicago, IL), or at *Centro Cardiologico Monzino* (Milan, Italy) undergoing clinically indicated RT3-D TEE imaging were considered. The protocol was approved by the local Institutional Review Board, and informed consent was obtained from all participants.

RT3-D TEE studies were performed using the iE33 system (Philips Medical Systems, Andover, MA, USA) equipped with fully sampled matrix-array transesophageal echocardiography (TEE) transducer (X7-2t): The probe was positioned at the midesophageal level with a 120° tilt and images acquired using the wide-angled
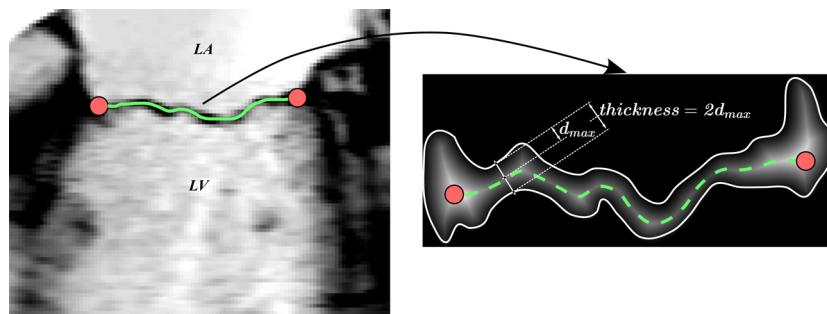

Fig. 5. The computed leaflet medial axis between a pair of annular points (left) and the estimation of leaflet thickness from the corresponding distance transform (right).
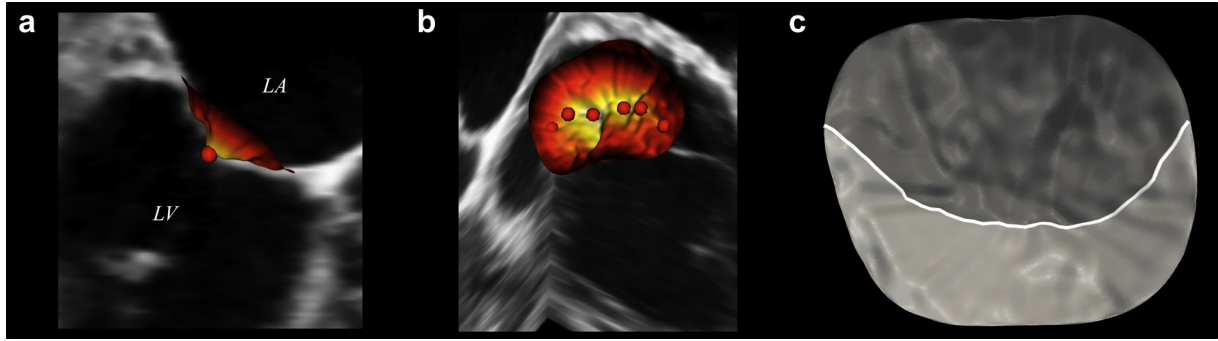
Fig. 6. Semiautomatic detection of the coaptation line, and anterior and posterior mitral leaflets. (a) A cut-plane of the original volume together with the ML mesh, where color overlay represents the local tenting height (from black—lower values—to yellow—higher values). The red point, selected by the user, matches the local maximum (yellow region) of the local tenting height. (b) The complete set of points selected by the user and passing through the CL using the original volume and the tenting regional distribution as reference. (c) The CL is automatically constructed from the set of selected points (white curve) and the A and P ML are automatically extracted from the initial ML mesh (dark and light gray surfaces).

acquisition mode, in which ECG-triggered wedge-shaped sub-volumes were obtained over four or seven consecutive cardiac cycles (volume rate 15–20 Hz). The scan volume in the wide-angled acquisition mode was optimized to include the mitral apparatus, the aortic valve and proximal ascending aorta, while excluding the mid and apical ventricular segments to maximize frame rate. Gains and compression were optimized in each patient, and kept constant during the acquisition. The acquired 3-D data set's dimension in the reformatted Cartesian range was roughly $200 \times 200 \times 200$ voxels with a voxel resolution ranging from 0.2 to 1.0 mm.

A group of 33 patients (50 ± 10 y) was considered for validation purposes. Specifically, it was composed of: (i) 9 patients with normal left-ventricular volume and mitral apparatus (NL); (ii) 12 patients with dilated cardiomyopathy (DCM), presenting global left ventricular dysfunction and dilation; (iii) 12 patients (MVR) with degenerative MV disease and severe mitral regurgitation that underwent MV repair with conventional surgical techniques on the ML and with implantation of partial annular rings on the posterior leaflet. Voxel resolution of each RT3-D TEE data set ranged from 0.2 to 1.0 mm.

The accuracy of the proposed algorithm was tested as follows:

1. MA and ML automated segmentations were compared point-to-point on the same stack of rotational cut-planes with manual tracings performed by an expert cardiologist, assumed as the "gold standard," by computing Euclidean distances expressed in pixels in 2-D space; in the case of ML, the manual tracing corresponds to the center line of the leaflets, as seen by the expert. For ML comparison, a spline interpolation was applied on the set of automatically computed tracings, to ensure that each ML medial axis contained the same number of points as in the manual tracings. Moreover, to test for reproducibility of the "gold standard" measurements, the same expert, blinded to previous results, repeated the tracings after 6 mo. Intra-observer variability for the computed parameters was evaluated using the coefficient of variability (CV) (defined as the ratio of the SD of the pair of manual measures as a percent of their mean), Bland-Altman analysis (with corresponding limits of agreement) and Pearson correlation coefficient (r).

2. To validate the accuracy in the computation of the regional thickness and regional tenting height of the ML, the same set of radial cut-planes and corresponding automatic and manual tracings was used. For each pair of corresponding radial cut-planes and tracings, the local 2-D thickness and tenting of leaflets was computed, then corresponding errors were obtained in pixels.

3. A parametric map of local error distributions was obtained for each data set, and then combined to compute a parametric map of median errors in the N group through a remapping operation onto the unit disk.

4. CL semiautomated segmentations were compared with manual tracings performed by an expert. To do so, a set of parallel cut-planes going from Al to Pm annular points was obtained, with the distance between two consecutive planes equal to 1.5 mm. For each of these planes: (i) the expert selected the coaptation point (gold standard), and (ii) the intersection between the plane and the CL computed semiautomatically was obtained, (iii) the point-to-point Euclidean distance between the points obtained in (i) and (ii) was computed, representing the accuracy of the semiautomated procedure.

5. Moreover, to test for the reproducibility of the "gold standard" CL measurements, the same expert, blinded

to previous results, repeated the selection of the coaptation points. For each set of points, the coaptation line length (defined as the cumulative sum of the distances between consecutive points defining the CL) was computed, and intra-observer variability was assessed using the coefficient of variability, Bland-Altman analysis (with corresponding limits of agreement) and Pearson correlation coefficient (*r*).

To test the reproducibility of the morphologic parameters obtained from both the MA and ML 3-D representations, in terms of their inter-observer variability, two operators, blinded to each other, analyzed separately all the normal patients in the data set with the proposed method. To test for intra-observer variability, the first operator repeated the analysis twice. Variability for both inter- and intra-observer was evaluated using the coefficient of variability (CV) (defined as the absolute difference between the pair of measures in percent of their mean), Bland-Altman analysis (with corresponding limits of agreement) and Pearson correlation coefficient (*r*).

To show the applicability of our approach in the clinical setting, an additional set of nine patients (52 ± 12 y) with a variety of MV morphologies was included: One patient with normal (NL) valve dimensions, one with DCM and annular dilation, one with MVR after annuloplasty, one with rheumatic MV stenosis (MVS) with mild annular calcification and increased leaflet thickness, three patients with ML perforation resulting from bacterial endocarditis, and two patients with ML malcoaptation.

Implementation of the algorithm

Software for manual navigation of the 3-D data and initialization was implemented using C++ and the Visualization Toolkit–VTK (Kitware Inc., New York, NY, USA). The initialization procedure (*i.e.,* user delineation of nine points) required less than one min on average, including data retrieval and choice of correct planes. The core algorithm for MA and ML segmentation and quantification was implemented in Matlab (The Mathworks Inc., Natick, MA, USA) and computation time was about 50 s on a 2 GB RAM, 2.26 GHz Intel Core Duo Laptop. Complete characterization of MA and ML global and regional morphology thus took approximately 2 min on average for each data set.

RESULTS

Validation

All acquired 3-D images were suitable for analysis, as they did not present any stitching or dropout artifacts. The generation of the "gold standard" involved a total of 1188 2-D tracings (36 leaflet trac-

ings and 72 MA points for each of the 33 patients) to be used for comparison, and took about 10 min/data set. Table 1 shows the computed intra-observer vari-ability of the "gold standard" both for MA and ML parameters in the NL group, and Figure 7 shows a representative example of the corresponding Bland-Altman analysis. Most of the computed parameters exhibited a high reproducibility (CV less than 10%and coefficients of correlation above 0.9), except for the MA height, the ML tenting volume and the ML mean tenting height (with CV values close to 15%and correlation coefficients equal or less than 0.8).

Figure 8 shows the regional distribution of the median error (Euclidean distances) in mm between the manual and automated results relevant to the annular contour points location, counter-clockwise along the annular profile (from Al to Al), computed for the 33 patients. It is possible to notice the globally reduced median error of 0.7 mm (25% and 75%: 0.7 and 1.4 mm, respectively) along the MA contour, showing the good performance of the automated detection algorithm. In particular, slightly higher distances (between 0.7 and 1.2 mm) were observed near the A point, compared with regions between Al and Pm points (between 0 and 1.0 mm).

The errors in ML segmentation (Fig. 9, first row) are comparable among populations, and range from 0 to 1.6 mm, with a median error of 0.6 mm (with 25% and 75% percentiles of 0.2 and 1.0 mm, respectively) for the entire data set. In MVR, slightly higher errors around

Table 1. Results of the reproducibility analysis in the normal subgroup (n = 9) for the measured MV morphologic parameters obtained using manual tracings. Mean value of the two tracing sessions performed by the expert cardiologist, together with the coefficient of variation (CV), bias ± 2 SD from Bland-Altman analysis (BA) and Pearson correlation coefficient (r)

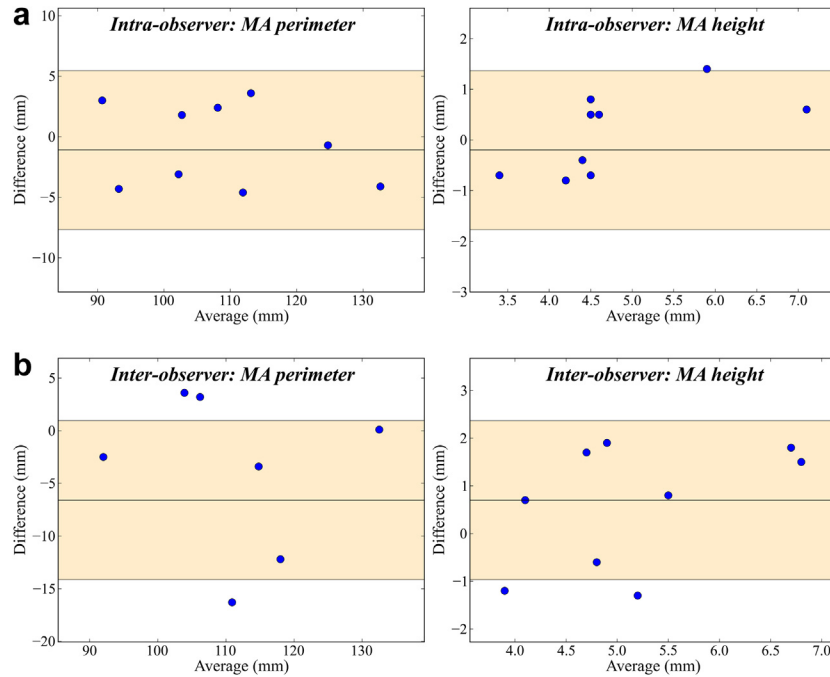| Parameter	Mean ± SD	Intra-observer variability		
		CV (%)	BA	r
MA perimeter (mm)	112.8 ± 12.3	3.7 ± 2.1	0.6 ± 5.2	0.95
MA A-P diameter (mm)	32.0 ± 4.6	4.2 ± 1.9	0.8 ± 3.2	0.96
MA Al-Pm diameter (mm)	37.6 ± 5.2	4.3 ± 3.2	0.5 ± 3.8	0.95
MA height (mm)	4.8 ± 2.0	15.2 ± 3.9	0.2 ± 2.2	0.81
MA 3-D surface (cm^2)	9.5 ± 2.2	8.1 ± 3.1	0.3 ± 2.3	0.92
MA 2-D surface (cm^2)	8.8 ± 2.4	6.6 ± 3.7	0.2 ± 1.9	0.95
ML 3-D surface (cm^2)	16.2 ± 3.5	11.3 ± 4.0	0.6 ± 2.2	0.86
ML mean thickness (mm)	2.6 ± 1.1	3.4 ± 2.4	−0.1 ± 0.3	0.99
ML tenting volume (mL)	1.1 ± 0.6	13.3 ± 6.9	0.1 ± 0.5	0.73
ML max. tenting height (mm)	5.0 ± 1.4	10.7 ± 8.3	0.2 ± 0.9	0.74
ML mean tenting height (mm)	1.3 ± 0.8	14.1 ± 5.5	−0.1 ± 0.7	0.84

Fig. 7. Representative Bland-Altman plots for the reproducibility of the morphologic parameters for: (a) Intra-observer variability; (b) Inter-observer variability. The parameters depicted exhibit the lowest (MA perimeter) variability and highest (MA height) variability.

the posterior annular region were observed, given the presence of suture points as a result of the annuloplasty procedure. In NL, slightly higher errors around the anterior annular portion were also visible.

The median of signed errors for thickness and tenting computation (Fig. 9, second and third rows) show values of -0.1 mm (-1.2; 1.0 mm), and of 0.2 (-1.3; 1.2 mm), respectively for these two regional parameters. Again, in NL a slightly higher tenting height overestimation, located toward the left half of the map and reflecting the positioning error shown in the ML segmentation around the anterior region, was visible. Also in MVR

this behavior was present, but with higher errors in thickness and tenting around the posterior annular portion, as a result of the presence of suture points mentioned previously.

Table 2 shows the computed inter- and intra-observer variability, both for MA and ML parameters in the NL group. The proposed algorithm showed a good level of reproducibility for most of these parameters. In particular, intra-observer reproducibility was high (CV values close to 10% and correlation coefficients higher than 0.95) for annulus perimeter, A-P and Al-Pm diameters as well as for surfaces and mean thickness. Conversely, height,
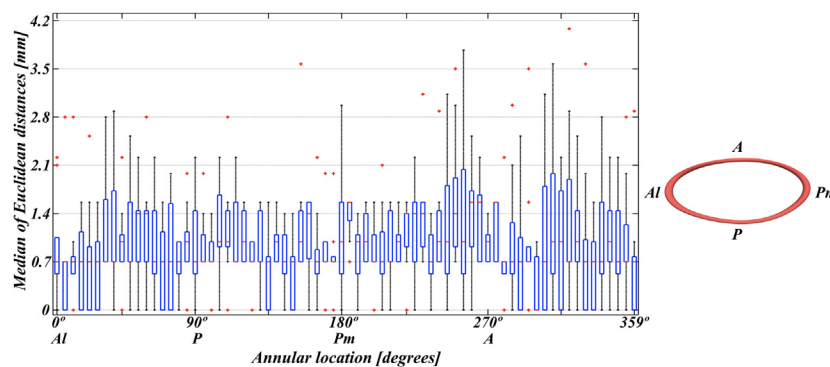

Fig. 8. Box and whisker plots (represented as median, first and third quartiles) for the regional error distribution in the MA segmentation algorithm versus manual tracings. The corresponding anatomic locations on the MA are depicted on the right.
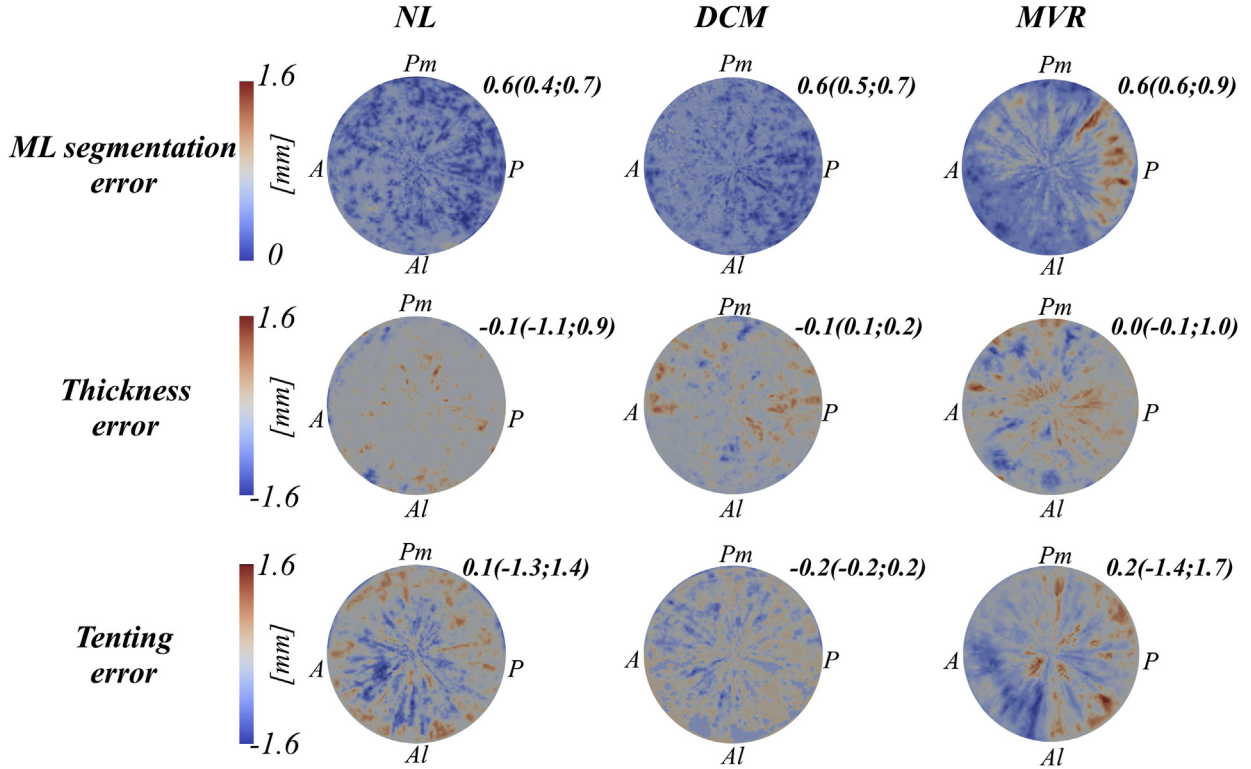
Fig. 9. Parametric maps of regional error distribution for the ML segmentation and quantification algorithms. From left to right: NL, DCM and MVR groups. From top to bottom: ML segmentation error, thickness error and tenting error. The same color scale has been used for each variable to allow comparisons between groups.

tenting volumes and maximum and average tenting heights were found as the least reproducible (CV around 20% and correlation coefficients below 0.9).

Figure 10 shows the accuracy (Euclidean distances) of the CL segmentation algorithm in the NL group, with values ranging from 0.8 to 1.9 mm and a mean error of 1.1 ± 0.5 mm for the entire data set. In addition, Table 3 shows the computed intra-observer variability of the CL length measurement, both for the gold standard

and for the semiautomatic CL segmentation algorithm; reproducibility of this measurement resulted high and similar in both cases (CV and r close to 11% and 0.95, respectively).

Clinical applicability

The potential applicability of the proposed approach in clinical practice was preliminarily explored by analyzing patients with different MV pathologies.

Table 2. Reproducibility analysis for the MV semi-automatic segmentation algorithm in the normal subgroup (n = 9). Mean value of the two observers is reported, together with the coefficient of variation (CV), bias ± 2 SD from Bland-Altman analysis (BA) and Pearson correlation coefficient (r)

| Parameter	Mean ± SD	Intra-observer variability			Inter-observer variability		
		CV (%)	BA	r	CV (%)	BA	r
MA perimeter (mm)	111.1 ± 14.3	3.0 ± 1.3	−1.1 ± 6.7	0.97	6.0 ± 4.8	−6.6 ± 7.7	0.93
MA A-P diameter (mm)	29.4 ± 4.0	4.0 ± 2.4	0.6 ± 2.4	0.97	8.8 ± 6.6	−2.4 ± 4.5	0.83
MA Al-Pm diameter (mm)	37.8 ± 5.5	3.9 ± 2.7	0.2 ± 3.4	0.96	9.1 ± 7.6	−3.2 ± 6.7	0.84
MA height (mm)	5.0 ± 1.2	12.1 ± 5.4	−0.2 ± 1.6	0.84	19.1 ± 7.0	0.7 ± 1.7	0.73
MA 3-D surface (cm^2)	9.1 ± 2.5	7.4 ± 4.6	0.4 ± 1.9	0.91	12.8 ± 9.8	−1.3 ± 2.4	0.96
MA 2-D surface (cm^2)	8.6 ± 2.5	6.1 ± 4.7	0.2 ± 1.5	0.95	11.8 ± 7.2	1.1 ± 2.0	0.97
ML 3-D surface (cm^2)	13.5 ± 3.0	8.1 ± 3.8	−0.2 ± 2.8	0.88	13.5 ± 9.3	−1.9 ± 2.8	0.90
ML mean thickness (mm)	2.6 ± 0.9	3.5 ± 2.6	0.1 ± 0.2	1.00	6.4 ± 5.8	−0.2 ± 0.5	0.99
ML tenting volume (mL)	1.3 ± 0.2	11.5 ± 6.3	0.1 ± 0.3	0.75	17.3 ± 7.3	−0.2 ± 0.3	0.89
ML max. tenting height (mm)	5.0 ± 0.9	9.4 ± 13.5	−0.1 ± 1.5	0.74	18.0 ± 9.9	0.3 ± 2.2	0.81
ML mean tenting height (mm)	1.6 ± 0.5	11.1 ± 8.9	0.1 ± 0.5	0.88	16.8 ± 7.6	0.2 ± 0.7	0.82
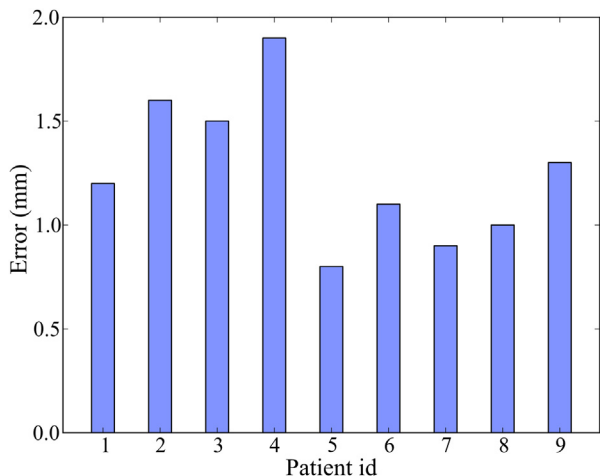
Fig. 10. Coaptation line segmentation error in the normal group (n = 9).

Table 4 summarizes the resulting morphologic parameters in the NL, DCM, MVR (a patient with P2 prolapse with chord rupture, undergoing posterior leaflet resection and Cosgrove ring implant; Edwards Lifesciences LLC., Irvine, CA, USA) and MVS patients. In addition, Figure 11 depicts the atrial view of the 3-D models with the corresponding tenting height and leaflet thickness parametric color maps using the same scale and voxel resolution.

As seen in Table 4, the DCM patient exhibits a larger, dilated MA compared with the subject with normal MV. Conversely, as a result of the annuloplasty procedure, the MA dimensions in the MVR patient were reduced, together with higher tenting near the CL (Fig. 11c). Compared to the normal MV (mean thickness 2.1 mm), increased thickness is visible both in the DCM (2.8 mm) and in the rheumatic (3.3 mm) patient, with areas of higher values (up to 6 mm) localized onto the CL (Fig. 11f and 11h). Also, an increase in thickness is visible in the MVR patient (3.2 mm) in correspondence to the posterior leaflet, but not on the anterior

Table 3. Results of the reproducibility analysis in the normal group (n = 9) for the CL length obtained using manual tracings (gold standard) and the semiautomatic algorithm. On each case, mean values of the two observations are reported, together with the coefficient of variation (CV), bias ± 2 SD from Bland-Altman analysis (BA) and Pearson correlation coefficient (r)

		Intra-observer variability		
Parameter	Mean ± SD	CV (%)	BA	r
CL length from gold standard (mm)	47.1 ± 5.2	11.3 ± 2.9	2.5 ± 1.6	0.94
CL length from semiautomatic algorithm (mm)	48.0 ± 3.4	10.5 ± 2.1	2.1 ± 1.6	0.96

Table 4. Global and regional parameters for the morphologic characterization of mitral annulus and leaflets in a normal valve, a patient with dilated cardiomyopathy (DCM), a patient after mitral valve repair with annuloplasty (MVR) and a patient with mitral valve stenosis (MVS)

Patient parameter	Normal	DCM	MVR	MVS
MA perimeter (mm)	113.0	122.6	104.1	105.6
MA A-P diameter (mm)	31.3	34.7	26.4	25.9
MA Al-Pm diameter (mm)	36.9	38.3	34.3	35.7
MA height (mm)	5.6	5.0	4.3	4.6
MA 3-D surface (cm^2)	9.7	10.6	7.7	8.1
MA 2-D surface (cm^2)	9.3	10.3	7.6	7.9
ML 3-D surface (cm^2)	10.2	13.5	8.4	8.9
ML mean thickness (mm)	2.1	2.8	3.2	3.3
ML tenting volume (mL)	1.4	3.0	1.6	2.1
ML max. tenting height	4.8	5.7	5.6	5.1
ML mean tenting height	1.8	2.3	2.5	2.1

(Fig. 11g), as a possible effect of the surgical procedure (in this case it is also possible to note the presence of suture points near the P border of the implanted ring).

Figure 12 shows the 3-D volume rendering (top) of the RT3-D TEE data and the corresponding 3-D mesh (bottom) with leaflets thickness overimposed as a parametric color map, for the three patients with leaflet perforation (Fig. 12a-c) and the two patients with leaflets malcoaptation (Fig. 12d-e). It is possible to notice the direct match between the location of the perforation/malcoaptation, highlighted in the rendered volumes, and the corresponding zero-thickness regions (gray spots in Fig. 12, bottom) in the parametric images.

DISCUSSION

The recent introduction of RT3-D TEE has allowed improved description of the morphologic abnormalities of a variety of MV pathologies compared to the information provided by 2-D techniques. According to recent guidelines (Bonow et al, 2008), this technology should be currently regarded as a valuable adjunct to the standard 2-D examinations in decisions regarding MV repair (Pepi et al. 2006; Sugeng et al. 2008). Currently, quantitative analysis of the MV apparatus can be performed using custom-based or commercially available dedicated software (Chandra et al. 2011; Grewal et al. 2010; Suri et al. 2009; Veronesi et al. 2012; Khabbaz et al. 2012). The proposed approach minimizes user interaction for MA segmentation, and provides a complete automated segmentation of the ML, thus allowing the quantification of MA and ML morphologic parameters. The use of commercial software (Philips QLAB MVQ module) could require on average 7 to 10 min (Tsang et al. 2011; Maffessanti et al. 2011) to manually achieve MA and ML quantification (only global parameters one to seven, as listed in Section 2.5), it is
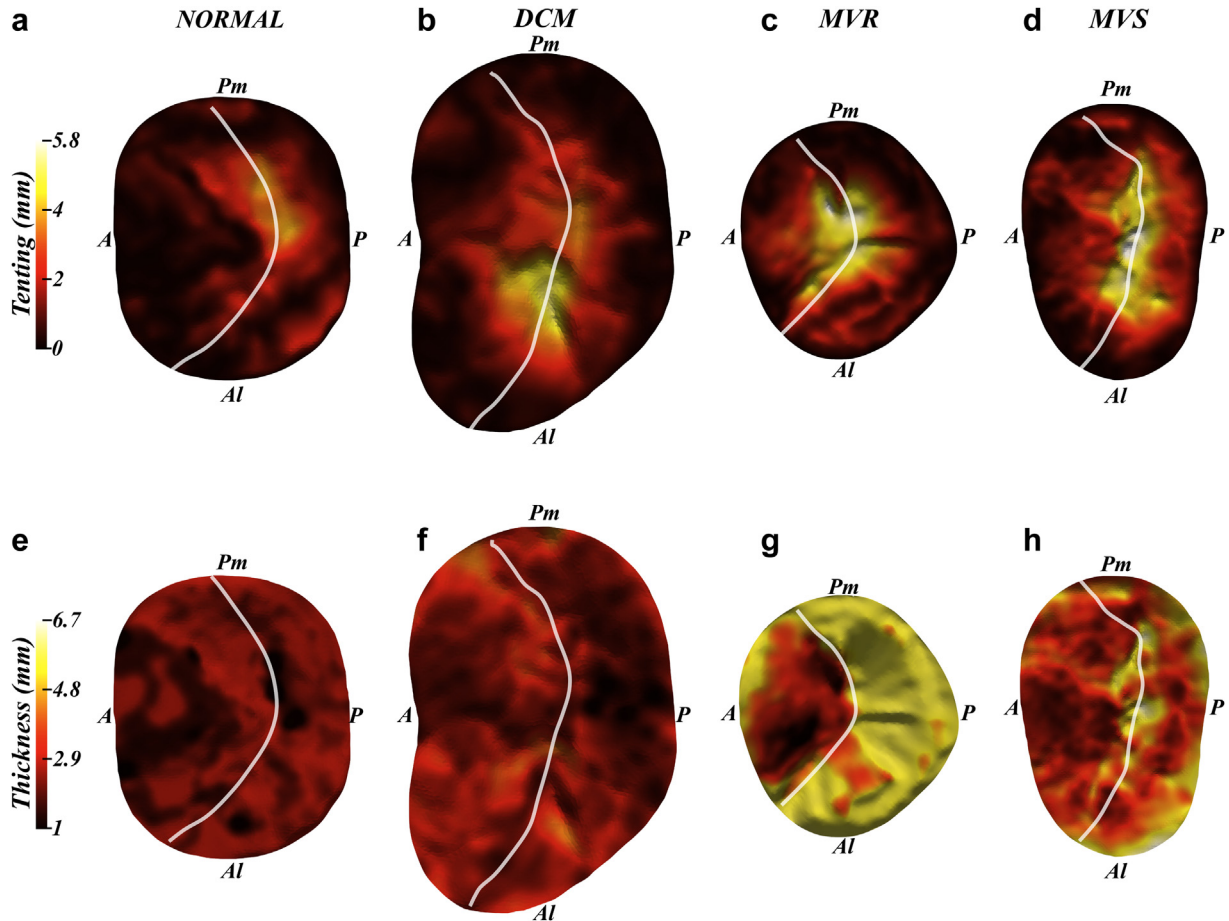
Fig. 11. MV 3-D representations (atrial views) with regional tenting (top) and thickness (bottom) patterns superimposed as color maps for a normal MV, and DCM, MVR and MVS patients. The white continuous line on each representation corresponds to the location of the coaptation line.

cumbersome, user-dependent and involves several initialization steps including the selection of A-P and Al-Pm annular points, of a couple of annular points on a set of six additional cut-planes (*i.e.,* 16 points to define the MV contour), and the manual tracing of the leaflet profile and coaptation points on multiple (between 12 and 18) parallel cut-planes from the Al to the Pm region (Maffessanti et al. 2011). In addition, no estimation of ML local thickness and tenting is provided, and no export of the quantified MV surface mesh is allowed.

On the contrary, our approach reliably quantifies both global and regional MA and ML morphology, with a much simpler initialization procedure (nine points) and reduced computation time (two min). Moreover, both annular contour and leaflet meshes are made avail-able for their potential additional utilization in patient-specific MV finite element modeling.

The dense angular sampling of the 3-D volume used for constructing the set of radial 2-D cut-planes (5° apart) ensures a high degree of spatial correlation between adjacent slices, thus adding robustness to the MA segmenta-

tion. Also, the introduction of a denser initialization of the MA anterior region (in total five user-defined points) improves the detection in correspondence to the aorto-mitral septum. As the MA and the anterior leaflet exhibit similar thickness on the fibrous tissue coupling the mitral and the aortic valves, the manual selection of one annular point only in this region could hamper the correct 3-D MA reconstruction.

Even with the use of WNCC (Fig. 3c), a metric insensitive to noise in the image (Nevo et al. 2007), the fundamental drawback of the forward tracking method is still present: the computed path tends to drift away from the optimal path once an error occurs. To overcome this limitation we introduced the junction-enhanced image which, along with the graph–search-based procedure, ensures that the annular regions will be correctly enhanced and detected once combined with the WNCC image (Fig. 3i).

Compared with previous semi-automated approaches (Schneider et al. 2010; Pouch et al. 2012; Burlina et al. 2010; Ionasec et al. 2010; Schneider et al. 2011; Mansi
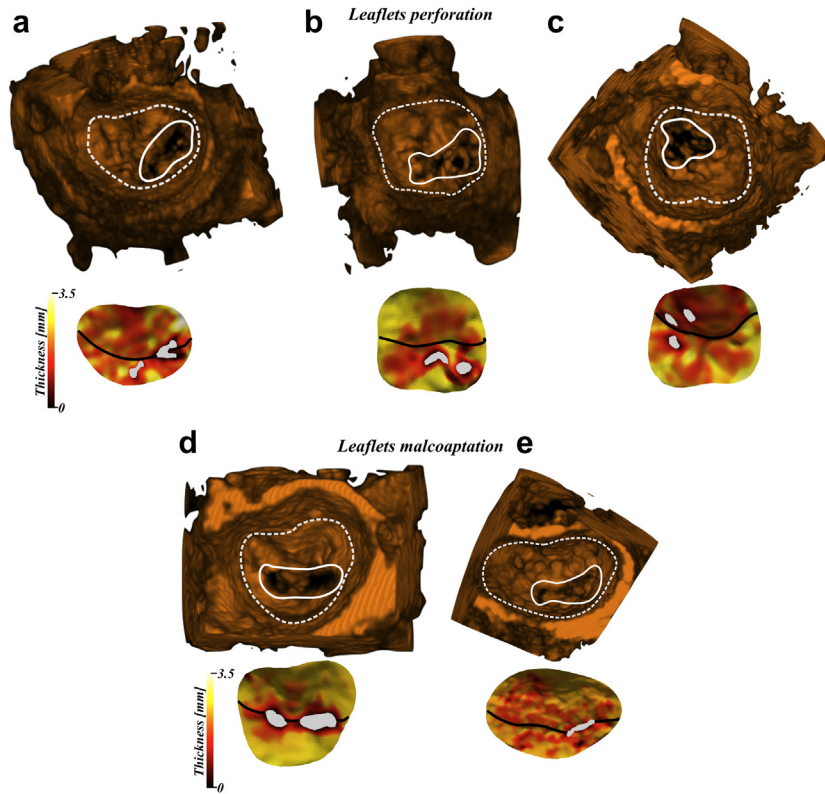
Fig. 12. MV 3-D volume renderings (top) and 3-D representations (bottom) for patients with leaflets perforations (a-c) and malcoaptation (d, e). The dashed and continuous contours in the rendered volumes represent the approximate locations of the MV and abnormalities, whereas the color scale on the left is the same for all representations. Black continuous lines in the 3-D representations correspond to the location of the CL.

et al. 2012), our method overcomes some of the existing limitations. In particular, we compute the leaflet thickness from the set of initialized cut-planes, which allows the computation of the JE image without any predefined thickness value; when combined with the WNCC and the 9 user-defined points, the Dijkstra algorithm allows the correct segmentation of the MA even in the anterior annular region. Conversely, in a previous approach (Schneider et al. 2010), a thin-tissue detector (TTD) based on a fixed leaflet thickness value was used to enhance the leaflets and locate the MV within the volume. Since the thickness distribution appears not to be uniform, and related to certain pathologic conditions, this constraint limits the clinical applicability of such analysis. In addition, the same TTD image is used to guide an evolving contour that segments the MA, corresponding to regions where the thin-tissue is attached to the thicker-tissue; the problem of this approach is that in the anterior annular region, in correspondence with the inter-valvular septum, it is difficult to differentiate the annulus from the leaflets, and thus the use of the TTD along with the active contour method may not always lead to accurate segmentations of the anterior annular portion. In spite of still relying on the thin-thick tissue junction hypo-thesis, our method overcomes the absence of such junctions

in the anterior annular portion by specifically including 5 initialization points in this region.

Another advantage of our method regards the orientation of the MV within the volume: the definition of one point in the LA cavity during the initialization allowed us to analyze valves in virtually any orientation within the pyramidal RT3-D TEE volumetric data set. In previous studies (Pouch et al. 2012), proper orientation of the MV apparatus inside the acquired data set (*i.e.,* parallel to one of the volume's main axes) was a pre-requisite for the segmentation to be applicable.

The use of nine initialization points, requiring approximately one min of interaction, may seem cumbersome. However, the complexity added to the algorithm initialization translates in more accurate segmentation of both the MA and the ML, which in turn ensures a correct estimation of the related morphologic parameters (both global and regional). Other existing methods (Schneider et al. 2010; Burlina et al. 2010; Ionasec et al. 2010 and Mansi et al. 2012) require less or no initialization points at all; however reported errors (ranging between 1.2 and 5.0 mm) still prevent the use of such approaches as tools for reliably in quantifying the morphology of the MA and the ML.

Finally, in our formulation the only constraints in the MA segmentation are the ROS and ROI sizes (which in spite of imposing a curvature constraint in the curva-ture of the segmented MA, still allow reduced segmen-tation errors, below 1.6 mm, as mentioned in Sec. 3.1) and the connectivity in the detection of 3-D annular points, whereas ML segmentation relies on 2-D graph connectivity: This resulted in adequate patient-specific segmentations both in normal and pathologic patients. In contrast, previous approaches (Burlina et al. 2010; Ionasec et al. 2010; Schneider et al. 2011; Mansi et al. 2012) were model-based, with the advantage of computing the MV configuration during the complete cardiac cycle (from diastole to systole), but with the drawback of using geometric, morphologic or mechani-cal priors that make the model not flexible enough on pathologic cases. Besides, the reproducibility of such approaches is limited, given the dependency on the particular data set available when the model was constructed.

Validation

Reproducibility analysis for the gold standard and for the semi-automated method showed comparable levels of variability. In particular, as seen in Tables 1, 2 and 3, the variability of the results obtained with the method (both CVs and coefficients of correlation) is lower than the gold standard inter-observer variability for all the computed parameters.

The comparison with manual tracings performed on the 33 patients showed a good performance in terms of accuracy for both MA and ML detection. In particular, the normalized regional error between corresponding MA point locations was minimal, and below 1.6 mm around the MA. These results are of the same magnitude as those previously reported by Schneider et al. (2010), where root mean square errors and mean normalized dis-tances, computed globally and not regionally, were of the order of 1.87 mm and 1.1 mm, respectively, for voxel sizes in the range 0.5–0.75 mm. Also the comparison of the corresponding ML point locations between the manual and automated segmentation resulted in a median error of the order of 0.6 mm, thus confirming the robust-ness of the unsupervised spatial fuzzy segmentation algo-rithm in the computation of the ML medial axis.

The use of the parametric maps of median errors applied to the validation of regional thickness and tenting height parameters evidenced minimal signed errors, with local positive errors (between 0.8 and 1.6 mm) in tenting height toward the anterior region in the NL group, prob-ably as a result of the fact that local errors in both segmen-tations of MA and ML affect cumulatively the tenting height computation. In both cases (thickness and tenting) an almost uniform distribution of signed errors around the

positive and negative values was found, thus implying that there is not systematic bias toward under or over-estimation of the computed parameters.

With regard to the repeatability of the analysis, our results showed a good inter- and intra-operator reproduc-ibility, except for the annular height and the maximum and mean tenting heights. This finding is in agreement with Maffessanti et al. (2011), where repeatability of the manual measurements was investigated and the MA height was found to be the most variable parameter (inter: 17.2%; intra: 11.5%). The level of intrinsic variability in this parameter is probably related to the spatial resolution of the acquired image, which in case of 1 mm resolution represents up to 20% of the mean annular height value (Tables 1 and 2).

Clinical applicability

Clinical value of the computed parameters. Previous studies (Caiani et al. 2011; Chandra et al. 2011; Maffessanti et al. 2011) have stressed the importance of the quantification of global annular dimensions and leaflet area (parameters one to seven in Sec. 2.5) for the ac-curate classification of the causes of MV disease and for the determination of the course of treatment in such cases. In addition, we hypothesized that ML local thick-ness and local tenting quantification, and the correspond-ing derived parameters (eight to 11 in Sec. 2.5) extracted from the 3-D echo data sets, could become an additional tool to improve the patients' diagnosis and to allow a deeper understanding of the etiology of the MV disease. In literature, some studies where the clinical rele-vance of similar parameters was studied are present: By using the 4-chamber view in conventional 2-D echocar-diographic imaging, with thickness being estimated in a single mid-point of each leaflet (both anterior and poste-rior), Chaput et al. (2008) demonstrated an increase in leaflets' size (area, length and thickness) in a group of pa-tients with DCM, in agreement with the result obtained in an ovine model (Dal-Bianco et al. (2009)). They also concluded that, in DCM, the ML undergoes a long-term adaptation following LV and MA dilation, thus underlin-ing the need to better understand the mechanisms behind this process as part of future therapeutic approaches. Rausch et al. (2012) found similar results after inducing chronic LV dilation in a sheep model and measuring leaf-lets area and strains, stressing the importance of quanti-fying thickness changes, to be correlated with the degree of MV regurgitation. Using RT3-D echocardiog-raphy, Anwar et al. (2010) proposed and validated a new score that includes ML thickness quantification for the assessment of patients with mitral stenosis. However, a limitation of such an approach was that thickness is quantified for a particular ML location from 2-D

cut-planes, thus making the results dependent on the chosen location.

In regard to tenting volume, several studies (Watanabe et al. 2005; Ryan et al. 2007) have shown that changes in the MA configuration lead to modifications in the 3-D ML tenting distribution, obtained by manual analysis of the RT3-D data sets, thus suggesting that this additional information could improve both the diagnosis and treatment of patients with MV disease. Also, the inaccuracy of single plane-based assessment, obtained by conventional 2-D echocardiographic techniques, for the effective and reproducible quantification of the degree of ML tethering, was proved.

Assessment of patients with different pathologies

The computed morphologic parameters for the normal MV group (Table 2) are consistent with those obtained in previous studies (Vergnat et al. 2011; Maffessanti et al. 2011; Grewal et al. 2010) describing the morphology of the MV in normal patients. Also, the measured ML thickness values are in agreement with those computed on 2-D apical 4-chamber view in 24 normal patients, as reported by Chaput et al. (2008). Different from previous work (Pouch et al. 2012; Burlina et al. 2010; Ionasec et al. 2010; Schneider et al. 2011), in which MA segmentation was applied using healthy and pre-operatory populations only, the proposed algorithm was able to correctly segment valves with different morphologies, including patients in post-operative stages, with global or local leaflet thickness changes, or partial malcoaptation.

In the DCM patient, as expected, the MV was deformed as a result of LV dilation, thus increasing MA and ML dimensions compared with normal valves (Table 4, third column). The reported tenting distribution as well as the increased leaflet thickness (Fig. 11) are consistent with previous studies (Chaput et al. 2008; Watanabe et al. 2005; Ryan et al. 2007), thus suggesting active adaptation process at cellular matrix level resulting in thicker anterior and posterior leaflets.

In the MVR patient, the MA segmentation correctly delineated the annulus, even in presence of the implanted ring (Fig. 11). The performed annuloplasty procedure induced several morphologic changes in the MV, in particular the undersizing of the MA that leads to an increase in tenting height as a result of the combined resizing of the leaflets, and the increased thickness in the posterior leaflet.

The analysis of the patient with rheumatic MV stenosis evidenced the expected thickening of ML (Table 4, fifth column), associated to this pathology, thus opening the possibility of using this regional infor-mation for improved score computation to define the proper surgical intervention. In fact, such patients are

nowadays addressed to MV replacement or percutaneous balloon dilation (*i.e.,* commissurotomy) based on Wilkins score (Wilkins et al. 1988) which includes thickness information computed from a single 2-D view.

The computed thickness patterns in patients with leaflet perforation and malcoaptation, along with the detection of the CL, allowed a correct identification of the local defects position, consistent with those depicted on the rendered volumes. The potential use of this information as a clinical tool would be the detection and quantification of the extent of damage in case of leaflet perforation, or the estimation of the surface of the regurgitant orifice in valves with malcoaptation.

Current limitations

The size of the population included in the study was limited. However, we aimed to test the accuracy and repeatability of the proposed measures, and to verify the applicability of this approach to several clinical cases characterized by different annular and leaflet morphologies. Future application to wider and selected patient groups would allow a better definition of potential changes in the computed parameters relevant to specific pathologies. In addition, the current implementation is not fully sensitive to prolapsed valves, and parameters such as CL length and tenting may not be directly correlated; in these pathologies semi-automated tracing would be necessary to allow ML segmentation. Moreover, algorithm's testing in presence of sub-optimal image quality was not assessed.

For validation, we did not use an independent ground truth but the manual tracings performed by an expert cardiologist on the 3-D echo data. This fact might not guarantee that the actual segmentations were correct.

We presented a semi-automatic procedure for the segmentation of the coaptation line, and included a preliminary validation of its accuracy and reproducibility. However, we did not analyze the clinical value of the CL length, and additional studies on different populations would be required to establish its clinical relevance.

Finally, our study was focused on static configuration of the MV (that is, considering only end-systolic frames), thus ignoring the dynamic changes in the MV apparatus that have been recently reported (Caiani et al. 2011; Grewal et al. 2010; Veronesi et al. 2012; Khabbaz et al. 2012; Veronesi et al. 2009).

CONCLUSIONS

We proposed a semi-automated algorithm for MA and ML segmentation from RT3-D TEE data, capable of characterizing the morphology of the MV with only 9-points user interaction, also including the computation of novel parameters, such as regional tenting height and

leaflet thickness. Validation compared to manual tracings showed small errors in segmentation, comparable with voxel resolution, and good reproducibility in the computed parameters.

Application to patients with different MV pathologies in pre- and post-operative stage, with global or local leaflet thickness changes or partial malcoaptation, showed the potential clinical utility of the proposed method, as well as its versatility in presence of completely different MV morphologies. The reported performance of the proposed fast, model-free, semi-automated MA and ML quantification makes it promising for future applications in clinical settings, where obtaining results rapidly is important such as in the operating room.

REFERENCES

Abdel-Dayem A, El-Sakka M. Fuzzy c-means clustering for segmenting carotid artery ultrasound images. Proceedings Image Analysis and Recognition 2007;935–948.

Amini A, Weymouth T, Jain RC. Using dynamic programming for solving varying problems in vision. IEEE Trans Pattern Anal Mach Intell 1990;12:855–867.

Anwar A, Attia W, Nosir Y, Soliman O, Mosad M, Othman M, Geleijnse M, El-Amin A, Ten Cate F. Validation of a new score for the assessment of mitral stenosis using real-time three-dimensional echocardiography. J Am Soc Echocardiogr 2010;23:13–22.

Bohs LN, Trahey GE. A novel method for angle independent ultrasonic imaging of blood flow and tissue motion. IEEE Trans Biomed Eng 1991;38:280–286.

Bonow RO, Carabello BA, Chatterjee K, de Leon AC Jr, Faxon DP, Freed MD. 2008 Focused update incorporated into the ACC/AHA 2006 guidelines for the management of patients with valvular heart disease. J Am Coll Cardiol 2008;52:e1–142.

Burlina P, Sprouse C, DeMenthon D, Jorstad A, Juang R, Contijoch F, Abraham T, Yuh D, McVeigh E. Patient-specific modeling and analysis of the mitral valve using 3-D-TEE. Inf Process Computer-Assisted Interventions 2010;135–146.

Caiani EG, Fusini L, Veronesi F, Tamborini G, Maffessanti F, Gripari P, Corsi C, Naliato M, Zanobini M, Alamanni F, Pepi M. Quantification of mitral annulus dynamic morphology in patients with mitral valve prolapse undergoing repair and annuloplasty during a 6-mo follow-up. Eur J Echocardiogr 2011;12:375–383.

Chandra S, Salgo IS, Sugeng L, Weinert L, Tsang W, Takeuchi M, Spencer KT, O'Connor A, Cardinale M, Settlemier S, Mor-Avi V, Lang RM. Characterization of degenerative mitral valve disease using morphologic analysis of real-time three-dimensional echocardiographic images: Objective insight into complexity and planning of mitral valve repair. Circ J Cardiovasc Imaging 2011;4:24–32.

Chaput M, Handschumacher MD, Tournoux F, Hua L, Guerrero JL, Vlahakes GJ, Levine RA. Mitral leaflet adaptation to ventricular remodeling. Circ J 2008;118:845–852.

Chuang K-S, Tzeng H-L, Chen S, Wu J, Chen T-J. Fuzzy c-means clustering with spatial information for image segmentation. Comput Med Imaging Graph 2006;30:9–15.

Dijkstra EW. A note on two problems in connexion with graphs. Numerische Mathematik 1959;1:269–271.

Grewal J, Mankad S, Freeman WK, Click RL, Suri RM, Abel MD, Oh JK, Pellikka PA, Nesbitt GC, Syed I, Mulvagh SL, Miller FA. Real-time three-dimensional transesophageal echocardiography in the intra-operative assessment of mitral valve disease. J Am Soc Echocardiogr 2009;22:34–41.

Grewal J, Suri R, Mankad S, Tanaka A, Mahoney DW, Schaff HV, Miller FA, Enriquez-Sarano M. Mitral annular dynamics in myxomatous valve disease: New insights with real-time 3-Dimensional echocardiography. Circ J 2010;121:1423–1431.

Ionasec R, Voigt I, Georgescu B, Wang Y, Houle H, Vega-Higuera F, Navab N, Comaniciu D. Patient-specific modeling and quantification of the aortic and mitral valves from 4-D cardiac CT and TEE. IEEE Trans Med Imaging 2010;29:1636–1651.

Khabbaz KR, Mahmood F, Shakil O, Warraich HJ, Gorman JH, Gorman RC, Matyal R, Panzica P, Hess PE. Dynamic 3-Dimensional echocardiographic assessment of mitral annular geometry in patients with functional mitral regurgitation. Ann Thorac Surg 2012;95:1–6.

Maffessanti F, Marsan NA, Tamborini G, Sugeng L, Caiani EG, Gripari P, Alamanni F, Jeevanandam V, Lang RM, Pepi M. Quantitative analysis of mitral valve apparatus in mitral valve prolapse before and after annuloplasty: A three-dimensional intra-operative transesophageal study. J Am Soc Echocardiogr 2011;24:405–413.

Mansi T, Voigt I, Georgescu B, Zheng X, Mengue EA, Hackl M, Ionasec R, Noack T, Seeburger J, Comaniciu D. An integrated framework for finite-element modeling of mitral valve biomechanics from medical images: Application to mitral-clip intervention planning. Med Image Anal 2012;16:1330–1346.

Muresian H. The clinical anatomy of the mitral valve. Clin Anat 2009; 22:85–98.

Nevo ST, van Stralen M, Vossepoel AM, Reiber JHC, de Jong N, van der Steen AFW, Bosch JG. Automated tracking of the mitral valve annulus motion in apical echocardiographic images using multidimensional dynamic programming. Ultrasound Med Biol 2007;33: 1389–1399.

Pepi M, Tamborini G, Maltagliati A, Galli CA, Sisillo E, Salvi L, Naliato M, Porqueddu M, Parolari A, Zanobini M, Alamani F. Head-to-head comparison of two- and three-dimensional transthoracic and transesophageal echocardiography in the localization of mitral valve prolapse. J Am Coll Cardiol 2006;48:2524–2530.

Pouch AM, Yushkevich P, Jackson BM, Jassar AS, Vergnat M, Gorman JH, Gorman RC, Sehgal CM. Development of a semi-automated method for mitral valve modeling with medial axis repre-sentation using 3-D ultrasound. Med Phys 2012;39:933–950.

Rausch M, Tibayan F, Craig D, Kuhl E. Evidence of adaptive mitral leaflet growth. J of the Mech Behav of Biomed Mat 2012;15: 208–217.

Ryan LP, Jackson BM, Parish LM, Sakamoto H, Plappert TJ, St John-Sutton M, Gorman JH, Gorman RC. Mitral valve tenting index for assessment of subvalvular remodeling. The Ann Thorac Surg 2007;84:1243–1249.

Schneider R, Perrin D, Vasilyev N, Marx G, del Nido P, Howe R. Mitral Annulus Segmentation From 3-D Ultrasound Using Graph Cuts. IEEE Trans Med Imaging 2010;29:1676–1687.

Schneider R, Burke W, Marx G, del Nido P, Howe R. Modeling mitral valve leaflets from three-dimensional ultrasound. Functional Imaging and Modeling of the Heart 2011;215–222.

Schneider R, Perrin D, Vasilyev N, Marx G, del Nido P, Howe R. Mitral annulus segmentation from four-dimensional ultrasound using a valve state predictor and constrained optical flow. Med Image Anal 2012;16:497–504.

Shewchuk JR. Mesh generation for domains with small angles. Proceedings of the sixteenth annual symposium on Computational Geometry 2000;1–10.

Song J-M, Fukuda S, Kihara T, Shin M-S, Garcia MJ, Thomas JD, Shiota T. Value of mitral valve tenting volume determined by real-time three-dimensional echocardiography in patients with functional mitral regurgitation. Am J Cardiol 2006;98:1088–1093.

Sotaquira M, Fusini L, Pepi M, Lang RM, Caiani EG. Quantitative characterization of mitral annulus and leaflets from transesophageal 3-D echocardiography. Proceedings of Computing in Cardiology 2013;233–236.

Sugeng L, Shernan SK, Weinert L, Shook D, Raman J, Jeevanandam V, DuPont F, Fox J, Mor-Avi V, Lang RM. Real-time three-dimensional transesophageal echocardiography in valve disease: Comparison with surgical findings and evaluation of prosthetic valves. J Am Soc Echocardiogr 2008;21:1347–1354.

Suri RM, Grewal J, Mankad S, Enriquez-Sarano M, Miller FA, Schaff HV. Is the anterior intertrigonal distance increased in patients with mitral regurgitation due to leaflet prolapse? Ann Thorac Surg 2009;88:1202–1208.

Tsang W, Weinert L, Sugeng L, Chandra S, Ahmad H, Spencer K, Mor-Avi V, Lang R. The value of three-dimensional echocardiography derived mitral valve parametric maps and the role of experience in the diagnosis of pathology. J Am Soc Echocardiogr 2011;24: 860–867.

van Stralen M, Leung K, Voormolen M, De Jong N, Van der Steen A, Reiber J, Bosch JG. Time continuous detection of the left ventricular long axis and the mitral valve plane in 3-D echocardiography. Ultrasound Med Biol 2008;34:196–207.

Vergnat M, Jassar AS, Jackson BM, Ryan LP, Eperjesi TJ, Pouch AM, Weiss SJ, Cheung AT, Acker MA, Gorman JH, Gorman RC. Ischemic mitral regurgitationa: Quantitative three-dimensional echocardiographic analysis. Ann Thorac Surg 2011;91:157–164.

Veronesi F, Caiani EG, Sugeng L, Fusini L, Tamborini G, Alamanni F, Pepi M, Lang RM. Effect of mitral valve repair on mitral-aortic coupling: A real-time three-dimensional transesophageal echocardiography study. J Am Soc Echocardiogr 2012;25:524–531.

Veronesi F, Corsi C, Sugeng L, Mor-Avi V, Caiani EG, Weinert L, Lamberti C, Lang RM. A study of functional anatomy of aortic-mitral valve coupling using 3-D matrix transesophageal echocardi-ography. Circ J Cardiovasc Imaging 2009;2:24–31.

Watanabe N, Ogasawara Y, Yamaura Y. Dynamics of mitral complex geometry and functional mitral regurgitation during heart failure treatment: Real-time three-dimensional echocardiographic study. J Echocardiogr 2006;4:51–58.

Watanabe N, Ogasawara Y, Yamaura Y, Kawamoto T, Toyota E, Akasaka T, Yoshida K. Quantitation of mitral valve tenting in ischemic mitral regurgitation by transthoracic real-time three-dimensional echocardiography. J Am Coll Cardiol 2005;45: 763–769.

Wilkins GT, Weyman AE, Abascal VM, Block PC, Palacios IF. Percutaneous balloon dilation of the mitral valve: An analysis of echocardiographic variables related to outcome and the mechanism of dilation. Br Heart J 1988;60:299–308.